Electrical detection of individual skyrmions in graphene devices

F. Finocchiaro, J. L. Lado, and J. Fernandez-Rossier

Phys. Rev. B **96**, 155422 — Published 9 October 2017

DOI: 10.1103/PhysRevB.96.155422

Electrical Detection of Individual Skyrmions in Graphene Devices

F. Finocchiaro[1], J. L. Lado[2] and J. Fernandez-Rossier[2,3]
[1] *IMDEA Nanociencia, Calle de Faraday 9, Cantoblanco 28049 - Madrid, Spain*
[2] *QuantaLab, International Iberian Nanotechnology Laboratory (INL), Av. Mestre Jose Veiga, 4715-310 Braga, Portugal and*
[3] *Departamento de Fisica Aplicada, Universidad de Alicante, San Vicente del Raspeig, 03690 Spain*
(Dated: September 15, 2017)

We study a graphene Hall probe located on top of a magnetic surface as a detector of skyrmions, using as working principle the anomalous Hall effect produced by the exchange interaction of the graphene electrons with the non-coplanar magnetization of the skyrmion. We study the magnitude of the effect as a function of the exchange interaction, skyrmion size and device dimensions. Our calculations for multiterminal graphene nanodevices, working in the ballistic regime, indicate that for realistic exchange interactions a single skyrmion would give Hall voltages well within reach of the experimental state of the art. The proposed device could act as an electrical transducer that marks the presence of a single skyrmion in a nanoscale region, paving the way towards the integration of skyrmion-based spintronics and graphene electronics.

I. INTRODUCTION

Skyrmions are magnetic non-coplanar spin textures that are attracting a great deal of attention for both their appealing physical properties[1] and their potential use in spintronics.[2–5] They have been observed forming lattices in a variety of non-centrosymmetric magnetic crystals,[6–9] including insulating materials such as the chiral-lattice magnet Cu_2OSeO_3.[10–12] They also form two dimensional arrays in atomically thin layers of Fe deposited on Ir(111).[13,14] In these systems the spins typically feel a competition between aligning with their neighbors and being perpendicular to them, what favors chiral ordering. A variety of interactions can assist non-collinear arrangements, including Dzyaloshinskii-Moryia interactions, dipolar interactions and frustrated exchange interactions and the size of an individual skyrmion can range from 1 nm to 1 μm depending on which specific mechanism is involved. To date, these magnetic structures are detected by means of neutron scattering,[6] electron microscopy[15] and even individually, with atomic scale resolution, by means of spin polarized scanning tunneling microscopy[13,16] and atomic size sensors.[17]

The particle-like nature of skyrmions has motivated proposals to use them as elementary units to store classical digital information, inspired by the magnetic domain-wall racetrack memories.[18] Such a perspective has become increasingly attractive since it has been experimentally proved[14] the possibility of manipulating two-dimensional magnetic lattices by creating and destroying individual skyrmions by means of spin-polarized currents in STM devices. This, along with the experimental finding[19] of skyrmion motion driven by ultralow current densities of the order of 10^{-6} A m^{-2}, considerably smaller than those needed for domain wall motion in ferromagnets, makes skyrmions potentially optimal candidates for the next generation of magnetoelectronic readout devices.

Mathematically, skyrmions are topologically non-trivial objects whose topology content is embedded in an index, the winding number N, defined as

$$N = \frac{1}{4\pi}\int_A \mathbf{n}(x,y)\cdot\left(\frac{\partial \mathbf{n}(x,y)}{\partial x}\times\frac{\partial \mathbf{n}(x,y)}{\partial y}\right)dx\,dy \quad (1)$$

where $\mathbf{n}(x,y):\mathbb{R}^2\rightarrow\mathbb{R}^3$ is a classical magnetization field and the two-dimensional integral is performed over the overall area occupied by the skyrmion. The winding number N can only acquire integer values, and a skyrmion is distinguished from other topologically trivial magnetic textures for exhibiting a non-zero value of the integer N. The magnetization field $\mathbf{n}(x,y)$ of a skyrmion can be expressed as a mapping from the polar plane coordinates $\mathbf{r}=(r,\phi)$ to the unit sphere coordinates (Φ,Θ)

$$\mathbf{n}(\mathbf{r}) = (\cos\Phi(\phi)\sin\Theta(r), \sin\Phi(\phi)\sin\Theta(r), \cos\Theta(r)) \quad (2)$$

provided the spin configuration at $r=\infty$ is ϕ-independent so that it can be mapped to a single point on the sphere. The mapping is specified by the two functions:[20]

$$\Phi(\phi) = N\phi + \gamma \quad (3)$$

and $\Theta(r)$ varies from 0 for large r to π as we approach $r=0$, the core of the skyrmion. Here we adopt the following model:

$$\Theta(r) = \begin{cases} \pi & \text{for } r=0 \\ f(r)=\pi\,(1-r/R) & \text{for } 0<r\leq R \\ 0 & \text{for } r>R \end{cases} \quad (4)$$

where N is the skyrmion winding number introduced in (1), γ is a phase termed helicity that can be gauged away by rotation around the z-axis, and $f(r)=\pi\,(1-r/R)$ is a function of the radial coordinate that describes a smooth radial profile inside of the skyrmion radius R. Such a texture describes a magnetic configuration where the spins are all aligned perpendicular to the film plane with the exception of those comprised within the radius R where they all progressively align along the anti-parallel

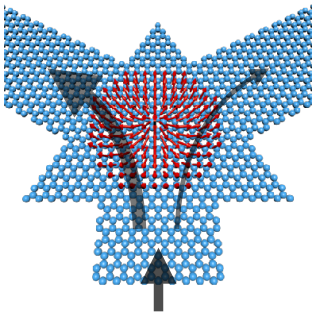

Figure 1. A graphene triangular quantum dot (the transmission region) proximized with a skyrmion and connected to three leads. Due to the anomalous Hall effect, a net transverse voltage is generated by the skew scattering of Dirac electrons traveling though the central region.

direction, that is picked up exactly at $r = 0$. The condition that the spins at $r = 0$ and $r = \infty$ are oppositely oriented is crucial in order to ensure a non-trivial topology of the magnetic texture.

Several recent theoretical works[21–23] point out that two-dimensional systems coupled either weakly or strongly to individual skyrmions or skyrmionic lattices can develop an Anomalous Hall (AH) or Quantum Anomalous Hall (QAH) phase owing to the non-trivial topology of these structures in real space. This effect refers to the onset of a transverse Hall response arising in magnetic systems driven by anomalous velocities, associated to Berry curvature, without the need of an applied magnetic field.[24] This anomalous Hall response can be either of extrinsic or intrinsic nature. In the case of proximizing a pristine 2D system with magnetic skyrmions, the generation of a transverse voltage is of extrinsic nature and ascribable to the imprinting of the skyrmions real space topology onto the (trivial) reciprocal space topology of the non-magnetic system,[23] and is known as the topological Hall effect. Based on these findings, along with a recent work demonstrating the possibility of growing a graphene flake on top of a single atomic layer of Fe on a Ir(111) substrate,[21,25] here we consider graphene flakes weakly coupled to magnetic films as skyrmion detectors. To this aim, we compute the skewness of the scattering and the associated Hall signal induced in a graphene island coupled to a single skyrmion within a multi-terminal geometry. Graphene unique properties are ideal to implement the proposed device. As a fact, being atomically thin maximizes proximity effects, making it an optimal material to grow on top of magnetic materials. Furthermore, the fabrication of high quality graphene electronic devices both at the micron and nanometer scale is absolutely well demonstrated[26–28] and its use as a magnetic sensor for magnetic adsorbates has been already tested experimentally[29,30] and studied theoretically.[31]

The paper is organized as follows. In section II we discuss a 2D Dirac system in the continuum coupled to a non-uniform spin texture and performing a standard rotation in spin space we unveil two types of influence on the Dirac electrons. In section III we introduce Landauer's formalism for quantum transport on the lattice and describe the setup of the proposed Hall experiment. Finally, in section IV, we discuss the results obtained by applying Landauer's formula to a graphene flake coupled to a single skyrmion, characterizing the Hall conductance as a function of several parameters and comparing the effectiveness of graphene with that of a standard two-dimensional electron gas (2DEG).

II. ANALYTIC APPROACH IN THE CONTINUUM

In this section we describe graphene electrons interacting with a non-coplanar magnetization field $\mathbf{n}$, as given by equation (2), using a 2D Dirac Hamiltonian:

$$H = H_0 + H_{ex} = -i\hbar\tau v_F \left(\partial_x\sigma_x + \tau\partial_y\sigma_y\right) + J\mathbf{n}\cdot\mathbf{s} \quad (5)$$

with $\mathbf{s} = (s_x, s_y, s_z)$ the vector of Pauli matrices acting in spin space and $\boldsymbol{\sigma} = (\sigma_x, \sigma_y, \sigma_z)$ the vector of Pauli matrices acting in pseudo-spin space. **Following the procedure introduced in previous works,**[20,21,32,33] we perform a rotation of the Hamiltonian so that in every point of space the spin quantization axis is chosen along the direction of the spin texture $\mathbf{n}$. As a result, the representation of the exchange term is diagonal in the rotated frame, but the Dirac Hamiltonian acquires new terms that encode the influence of the exchange interaction of the Dirac electrons with the non-coplanar field. This analytic model does not account for possible lattice mismatch effects between the graphene sample and the magnetic substrate, which could be responsible for valley mixing and/or coupling strength renormalization. In fact, the model is intended to qualitatively isolate the individual physical effects that sum up to give an anomalous response rather than providing an exhaustive description of the scattering problem. Microscopic effects at the lattice level will be included in the numerical tight binding approach that is the focus of the next section and in the appendix.

The unitary matrix $\mathcal{R}$ that performs the above-mentioned transformation in the basis $\psi = (A\uparrow, B\uparrow, A\downarrow, B\downarrow)^T$ is

$$\mathcal{R} = \begin{pmatrix} u & 0 & v & 0 \\ 0 & u & 0 & v \\ -v^* & 0 & u^* & 0 \\ 0 & -v^* & 0 & u^* \end{pmatrix} = \begin{pmatrix} u & v \\ -v^* & u^* \end{pmatrix}\sigma_0 \quad (6)$$

where

$$u = \cos\frac{\Theta(r)}{2}e^{i\Phi(\phi)/2} \quad v = \sin\frac{\Theta(r)}{2}e^{-i\Phi(\phi)/2} \quad (7)$$

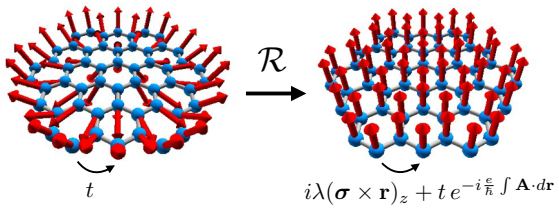

Figure 2. Mapping of a system characterized by real hopping and with a double exchange interaction with a non-coplanar magnetic texture to a system with spatially uniform magnetization field and with a complex hopping function mimicking the coexistence of spin-orbit with a vector gauge field.

The transformed Hamiltonian $H \to H' = \mathcal{R}H\mathcal{R}^{-1}$ reads

$$H' = \tau v_F \left[\sigma_x \left(p_x + \mathcal{A}_x\right) + \tau\sigma_y \left(p_y + \mathcal{A}_y\right)\right] + \\ + \frac{\hbar\tau v_F}{2}\left[-\sigma_x\left(\frac{N}{r}s_x n_y + \partial_r\theta s_y \cos\phi\right) + \right. \\ \left. + \tau\sigma_y\left(\frac{N}{r}s_x n_x - \partial_r\theta s_y \sin\phi\right)\right] + Js_z \qquad (8)$$

with

$$\mathcal{A}_x = \hbar\frac{N}{2r}\cos\theta\sin\phi\, s_z \\ \mathcal{A}_y = -\hbar\frac{N}{2r}\cos\theta\cos\phi\, s_z \qquad (9)$$

and $n_x = \cos\Phi\sin\Theta$, $n_y = \sin\Phi\sin\Theta$. In the rotated reference frame, the exchange term is manifestly diagonal. Besides, the Hamiltonian has acquired additional kinetic terms. The $\mathcal{A} = (\mathcal{A}_x, \mathcal{A}_y)$ field acts as a spin-dependent gauge vector potential that couples with the momenta of the Dirac electrons, whereas the remaining two terms closely resemble a spin-orbit (SO) interaction of the Rashba type. On the lattice, the above transformation corresponds to mapping a system characterized by a non-collinear exchange field and real hopping to a ferromagnetic system with a purely imaginary hopping mimicking the effect of SO coupling plus a complex hopping supported by a gauge field entering as a Peierls phase. This is schematized in figure 2. From the gauge field, one can compute the effective magnetic field acting on the system as

$$\mathcal{B} = \nabla\times\mathcal{A} = \hbar\frac{N}{2r}s_z\left[\partial_r\theta\sin\theta - \frac{1}{r}\cos\theta\right]\hat{z} \qquad (10)$$

that reads

$$\mathcal{B}_z = -\hbar\frac{N}{2r}s_z\begin{cases}\left[\pi\sin\theta/R + r^{-1}\cos\theta\right] & \text{for } r\le R\\ r^{-1} & \text{for } r > R\end{cases} \qquad (11)$$

This transformation of the Hamiltonian therefore allows to interpret the topological content embedded in the skyrmion texture as a superposition of two effects: (i) The generation of an effective emergent electromagnetic field (EEMF) described by the gauge potential $\mathcal{A}$; (ii) The coexistence of ferromagnetic exchange with a Rashba-like SO interaction, what has been predicted to give rise to a QAH phase.[34] Both ingredients are endowed with a topological character that the skyrmion texture is able to imprint onto the Dirac electrons and are therefore responsible for generating a Hall response in the system. **Expressions analogous to equations 8, 9 and 11 have been obtained in previous works in the context of Schrodinger and band electrons,[20,21,32,33] with the remarkable difference that in the strong coupling limit ($J \gg t$) the spin-mixing terms vanish and the problem is exactly mapped to a spinless one-band system where the electrons momenta are coupled to a vector potential describing an emergent magnetic field. In the case of Dirac electrons, the spin-mixing term survives at all coupling regimes and the mapping to a pure EEMF is an incomplete description of the physics taking place in the system.** Whereas this picture provides some physical insight of what happens to graphene Dirac electrons surfing a skyrmions, it does not provide a straightforward method to compute the Hall response.

III. TIGHT-BINDING QUANTUM TRANSPORT APPROACH

In this section we overview the quantum transport methodology that we will employ to compute the Hall response induced by an individual magnetic skyrmion in a graphene device. Importantly, we are implicitly assuming that the substrate material is an insulating skyrmion crystal such as $CuGeO_3$[35] and Cu_2OSeO_3[10–12] in such a way that the current only flows through graphene.

The graphene electrons are described with the standard tight-binding Hammiltonian for the honeycomb lattice with one p_z orbital per atom,[36] plus their exchange interaction with the classical magnetization of the skyrmion $\mathbf{n}$:

$$H = -t\sum_{<i,j>,\sigma} c^\dagger_{i\sigma}c_{j\sigma} + J\sum_i \mathbf{S}_i\cdot\mathbf{n}_i \qquad (12)$$

Here $\mathbf{n}_i$ is the classical continuous magnetization texture (2) discretized over the graphene lattice and taken at site i and $\mathbf{S}_i = \sum_{\sigma\sigma'} c^\dagger_{i\sigma}\mathbf{s}_{\sigma\sigma'}c_{i\sigma'}$ is the vector whose components are the Pauli matrices acting in spin space associated with the i-th lattice site. The $< i, j >$ symbol implies summation over all nearest neighboring pairs of atoms, and we are assuming that the magnitude of the magnetization is uniform over the whole graphene lattice. This Hamiltonian has been considered before[23] for the case of 2D graphene interacting with a skyrmion crystal. In contrast, here we consider a graphene device that hosts an individual skyrmion. We note that we are treating the rather complex interaction of the graphene carriers with the magnetic moments of the substrate as a purely local exchange interaction, as well as neglecting the modulation of the onsite potential associated to the

mismatch of the graphene lattice with that of the underlying material. While this is an approximation of the real problem, in the appendix we show that both assumptions are quite reliable as deviations from them do not yield considerable changes in the results presented in the main text.

The mathematical framework that we use to study quantum transport is based on Landauer's formalism for conductance.[37] Given an experimental setup where a device is attached to N metallic contacts, Landauer's multiterminal technique allows to compute the transmission amplitude between the m-th and the n-th contact from the relation

$$T_{mn} = \mathrm{Tr}\left(G_d^+ \Gamma_n G_d \Gamma_m\right) \tag{13}$$

where G_d and G_d^+ are respectively the retarded and advanced Green's functions of the device, that is the Green's function of the isolated device corrected by the self-energies Σ_m of the N leads

$$G_d^{-1}(\epsilon) = (\epsilon + i\delta)\,\mathbb{I} - H_d - \sum_{m=0}^{N-1} \Sigma_m \tag{14}$$

where H_d is the Hamiltonian of the isolated device. The Γ_m's are quantities associated to the leads' selfenergies as $\Gamma_m = i\left(\Sigma_m - \Sigma_m^+\right)$. The leads' self-energies incorporate the coupling between the device and the leads as $\Sigma_m = t_m^+ g_m t_m$, with g_m the surface Green's function[38] of the m-th lead, and t_m the hopping matrix between the device and the m-th lead. From the knowledge of the transmission amplitudes, the expression for the total current flowing from the lead m follows straightforwardly:

$$I_m = \frac{e}{h} \sum_{n \neq m} \int_{-\infty}^{+\infty} d\epsilon \left[f\left(\epsilon - \mu_m\right) - f\left(\epsilon - \mu_n\right)\right] T_{mn}(\epsilon)$$

with $f(\epsilon - \mu)$ the Fermi distribution function, so that at zero temperature the previous expression reduces to $I_m = \frac{e}{h} \sum_{n \neq m} \int_{\mu_n}^{\mu_m} d\epsilon T_{mn}(\epsilon_F)$ and for a sufficiently small energy interval $\mu_m - \mu_n$ one can expand the transmission coefficient $T_{mn}\left(\epsilon\right)$ around the Fermi energy ϵ_F and stick to zeroth order. By doing so, one finally finds that the formula for the current flowing from the lead m becomes:

$$I_m = \frac{e}{h} \sum_{n \neq m} (\mu_m - \mu_n) T_{mn}(\epsilon_F) \tag{15}$$

This equation can be used to derive the Hall response in a given multiterminal device in two different ways. In both cases, the first step of the calculation is the numerical determination of the transmission coefficients $T_{mn}\left(\epsilon\right)$. Then we can either impose (i) the voltage drops eV, defined as the difference between the chemical potentials of the different electrodes, and compute the resulting current (inverse Hall effect), or (ii) impose a longitudinal current flow and a null transverse current, find the resulting chemical potentials and determine the Hall response (direct Hall effect).

When the methods just described are implemented in an ordinary four-terminal geometry,[22] the resulting relation between the Hall conductance and the transmission coefficients is far from intuitive. In this paper, for the sake of simplicity, we consider a three terminal device (TTD) of the kind of the one shown in figure 3a. We choose to fix the chemical potentials of the three electrodes, labeled as 0, 1 and 2, and compute the resulting current. Specifically, we impose that $V_0 = V$ and $V_1 = V_2 = -V$. In this way, the voltage difference between leads 1 and 2 is automatically set to zero whereas the voltage difference between lead 0 and leads 1,2 is $V_y = V_0 - V_{1,2} = 2V$. The expression for the current flowing from leads 1 and 2 is $I_i = 2VT_{0i}$ for $i = 1, 2$. From this expressions it is straightforward to deduce the current imbalance δI, that reflects the presence of a transverse force, $\delta I = I_1 - I_2 = 2V(T_{01} - T_{02})$, whence our definition of Hall conductance in this geometry

$$G_H = \frac{\delta I}{V_0 - V_{1,2}} = \frac{e^2}{h}\left(T_{01} - T_{02}\right) \equiv \frac{e^2}{h}\delta T \tag{16}$$

In the following we present the numerical results for the normalized transmission imbalance, that is

$$T_H = \frac{\delta T}{T} \equiv (T_{01} - T_{02})/(T_{01} + T_{02}) \tag{17}$$

in order to work with quantities that do not depend on the number of conduction channels in the device. This 3-terminal setup simplifies considerably the analysis of the numerical results, and also matches the C_3 symmetry of the graphene lattice. However, in a real device, disorder and contact asymmetries might result in additional transmission imbalances that might obscure the detection of skyrmions. Thus, in real devices a standard 4 terminal geometry should be used, given that the principles and magnitude of the physical effect are expected to be the same.

IV. RESULTS AND DISCUSSION

We now present the results obtained by calculating the imbalance in the transmission coefficients T_H eq. (17) for a graphene quantum dot coupled to a skyrmion. For a better physical insight, we provide an estimate for the *equivalent* magnetic field B_{eq} that would give rise to a conventional Hall response of the same magnitude of that induced by the skyrmion. Details on the determination of such a field are given in the Appendix. In the following we consider flakes sizes of the order of $\sim$ 50 nm^2, and skyrmions with radius of the order of 2-3 nm and winding number $N = 1$. Also, we are solely interested in realistic[39,40] weak exchange proximity effects, that do not alter the graphene spectrum substantially, so we explore coupling constants up to $J \sim 100$ meV[40–42]. DFT calculations for graphene proximized with EuO,[40] $BiFeO_3$[41] and YIG[42] report exchange splittings on the order of 37,

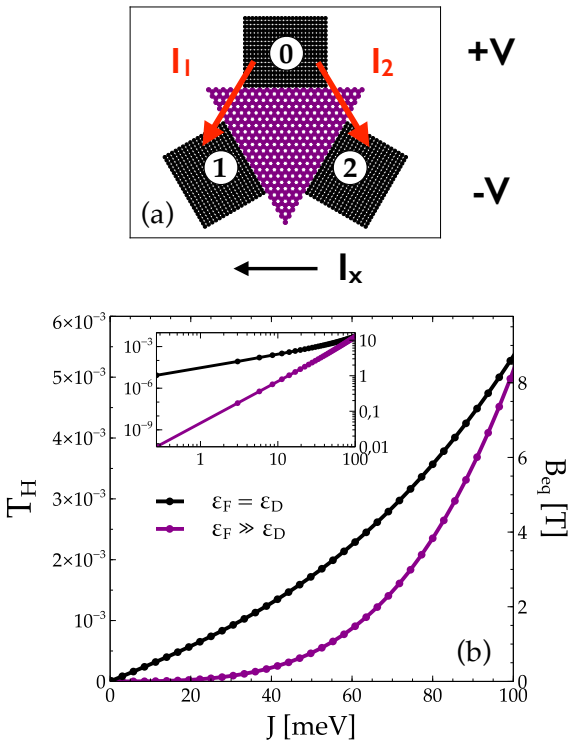

Figure 3. (a) Three terminal device setup for the inverse Hall measurement with C_3 rotational symmetry. (b) Normalized transmission imbalance T_H (eq. 17) and equivalent magnetic field B_{eq} as a function of the coupling constant J, comparison of a Dirac-like (undoped graphene, with the Fermi level ε_F close to the Dirac point) and a Schrodinger-like (heavily doped graphene, with ε_F much larger than the energy of the Dirac point ε_D) material for an island with side of 10.6 nm and a skyrmion radius of 2.3 nm. Inset: log-log representation of $T_H(J)$ and $B_{eq}(J)$.

70 and 50 meV, placing the range of coupling constants considered in our work fairly within the current state of the art. In order to simulate standard metallic contacts in some of the calculations square leads have been used instead of hexagonal leads. Results obtained with different leads geometries are consistent, so we chose to present curves associated to one or the other geometry in order to minimize resonance effects due to confinement inside of the central island. We note that as an anomalous current flows through the graphene dot, the magnetic skyrmion could undergo a current-driven rebound motion whose dynamics is governed by the Thiele's equation[43]. Such a phenomenon is beyond the scope of the present work, and we remit the reader to the several theoretical and experimental works[44–46] that focus on this topic for further details.

A. Anomalous Hall effect

We first investigate the magnitude and behavior of the transmission asymmetry T_H as a function of the coupling constant J, comparing the results for Dirac electrons (half filled honeycomb lattice, with the Fermi energy ε_F close to the Dirac point), and Schrodinger electrons (heavily doped honeycomb lattice, with the Fermi energy away from the Dirac point). The result is shown in fig. 3(b) in both linear and logarithmic scale, for a skyrmion with radius $R = 2.3$ nm and a device of linear dimension $L = 10.6$ nm. The first thing to notice is that, even for small $J \simeq 1$ meV, the equivalent field $B_{\rm eq}$ is of the order of 1 Tesla, which shows that the anomalous Hall effect is very large. For $J < 100$ meV the transmission imbalance T_H of Dirac electrons shows an approximately linear behavior with J in contrast with the case of Schrodinger electrons (Fermi energy away from the Dirac point) for which $\mathcal{T} \propto J^3$. For all the values of J, the Hall response for Dirac electrons is much larger than for Schrodinger electrons, most notably for the experimentally relevant case of small J, for which T_H is up to 4 orders of magnitude larger. This difference is reduced and eventually canceled at higher and unrealistic couplings larger than 100 meV.

We now characterize the Hall conductance of a graphene TTD by investigating its dependence on the system parameters, such as the Fermi energy of the leads, the skyrmion size R and the size of the graphene island coupled to the skyrmion. The results are shown in fig. 4. The anomalous Hall response as a function of the chemical potential of graphene (fig. 4(a,b)), shows a local maxima at charge neutrality, and other two local maxima of opposite sign at symmetric electron/hole doping, a behavior resembling graphene coupled to a skyrmion crystal.[23] Such phenomenology can be understood in terms of the modification of the Dirac cone due to the non-coplanar magnetization field. As we have seen in section II, the problem can be mapped to one where spatially uniform exchange field and Rashba-like spin-mixing terms coexist. The first contribution has the effect of lifting spin degeneracy, whereas the latter opens small gaps at both the Fermi energy and at crossing points forming at higher energies of the order of $\pm J$. Within these gaps, the absolute value of the Berry curvature reaches local maxima and this is reflected in the behavior of T_H as a function of the transmission energy ε shown in fig. 4.

In fig. 4(c) we show the behavior of T_H as a function of the skyrmion radius R, keeping the dimension of the device constant and equal to $L = 10.6$ nm, and $J = 80$ meV. We consider the case of small skyrmions with nanometric radius such as those found in systems with frustrated exchange interactions.[47] Two competing effects are at play as the radius of the skyrmion increases: on the one side the change in magnetization as a function of the distance from the skyrmion center becomes smoother, so that the effective skew scattering is weaker, and on the other the surface where the skew scattering

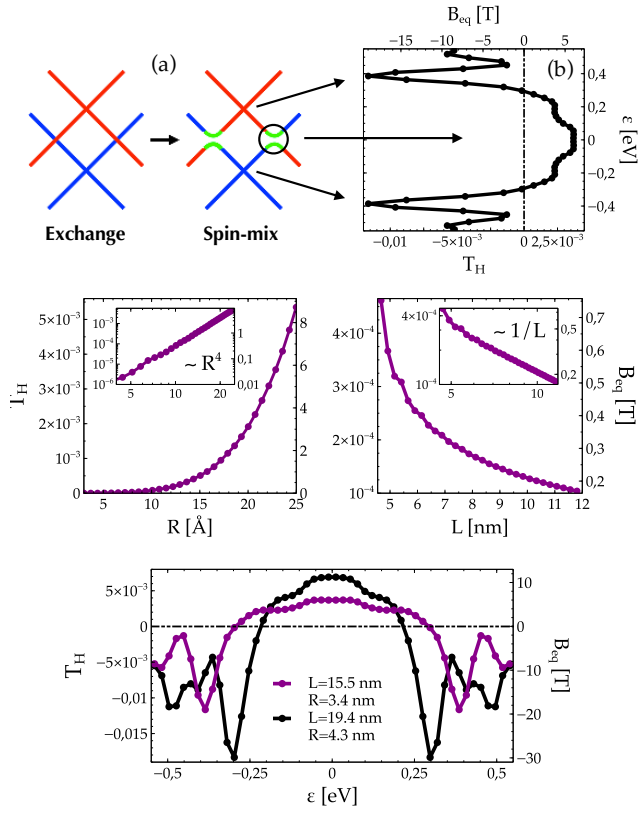

Figure 4. (a) Schematics of the effect on the local electronic structure of graphene of being proximized to a skyrmion. (b) Left-right normalized transmission imbalance T_H of a graphene TTD as a function of the transmission energy of the leads ε for an island of 15.5 nm, skyrmion radius of 3.4 nm and coupling constant $J = 80$ meV. Energies characterized by maximum absolute Berry curvature in the infinite system are evidenced. (c) and (d) Transmission imbalance of a graphene TTD as a function of skyrmion radius (with fixed flake size of $L = 10.6$ nm) and flake size (with fixed skyrmion radius of $R = 1.4$ nm), respectively. Both calculations have been performed for a coupling constant of 80 meV. Insets show log-log representation of T_H. (e) Comparison of two calculations where the radius of the skyrmion and the linear size of the flake are scaled linearly by a common factor $\alpha = 1.25$, for $J = 80$ meV. All plots present a second vertical axis in which the equivalent magnetic field B_{eq} is displayed.

is non zero increases. The normalized scattering asymmetry resulting from our calculations behaves as R^4 indicating that the second mechanism is dominant, and therefore that larger skyrmions yield a stronger Hall signal.

The dependence of the Hall response on the size of the graphene flake is shown in Fig. 4(d), for a fixed radius of $R = 1.4$ nm and an exchange of $J = 80$ meV. We see that by increasing the flake size while keeping the skyrmion radius fixed, the Hall signal decreases as L^{-1}, where L is the linear size of the triangular transmission region. From these results we infer that the Hall conductance behaves as $T_H(R, L) \sim R^4/L$ as a function of the radius and of the linear size of the central island. This scaling reflects the fact that the Hall response is proportional to the probability that the electrons surf over the skyrmion, which is manifestly an increasing function of R and a decreasing function of L.

By changing both the radius and the device size by a common factor α, T_H scales as $T_H(\alpha R, \alpha L) \sim \alpha^3 T_H(R, L)$ indicating that the Hall conductance is not scale invariant under simultaneous rescaling of R and L. Now, since we are considering flakes of the minimum experimentally achievable dimensions proximized with the smallest skyrmions experimentally detected so far (of the order of the nm, whereas observation of skyrmions with radius of up to 100 nm has been reported[15,48]), the presented scaling argument evidences that our estimates of Hall conductances of the order of 10^{-5}-10^{-4} G_0 merely set a lower bound for the range of values that this parameter can undertake in actual laboratory measurements. A general example of this non-linear scaling trend is shown in fig. 4(e) where a comparison of two systems with L and R scaled by a common factor is presented.

We note that most systems in the brink of hosting skyrmion lattices need a non-zero external magnetic flux to drive them into the skyrmionic phase, as they typically exhibit spiral spin phases at zero magnetic field. This implies that an additional non-zero Hall contribution is to be expected from the external field that sums up to the one driven by the skyrmion alone. An effective way to discriminate between the two effects relies on their different symmetry properties. In fact, while the skyrmionic contribution is electron-hole symmetric (as made clear by fig. 4(b)) and changes sign only by switching the sign of either J or N, the Hall effect induced by the magnetic field is electron-hole asymmetric as holes have opposite charge with respect to electrons and thus respond with an opposite velocity to an applied external magnetic field. It is thus the $\varepsilon \to -\varepsilon$ asymmetry of the overall scattering cross-section that allows to subtract the spurious external contribution and determine the intrinsic skyrmionic one. We also note that the anomalous Hall response will be non-zero if other non-coplanar spin textures, that are not skyrmions, are present in the background material. However, in most systems it is to be expected that the magnetic configurations that do not make it to the skyrmionic phase are structures that are coplanar but non-collinear, like spin spirals. Those kind of structures, because of coplanarity, are not able to generate an anomalous Hall signal in the absence of spin-orbit coupling.

B. Effects of disorder

So far we have dealt with a graphene flake perfectly clean. However, some current degradation brought about by defects or impurities in the sample is to be expected. In order to provide a more realistic estimate of the extent to which the Hall responses that our results anticipate

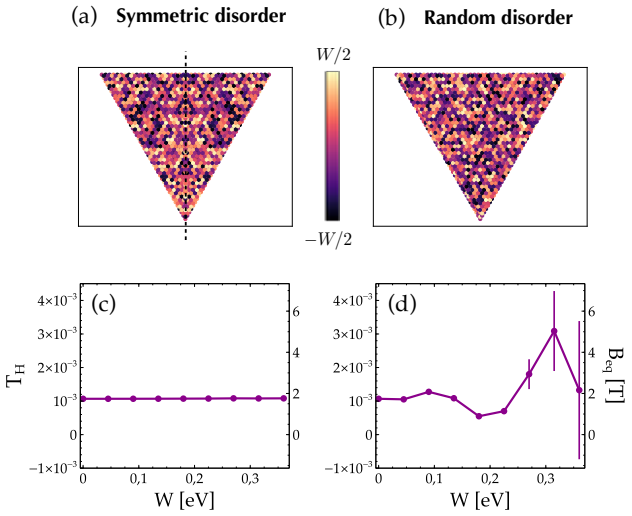

Figure 5. Panels (a) and (b) show a typical realization of a disordered configuration with (a) and without (b) $y \to -y$ symmetry. In panels (c) and (d) we present the associated curves of T_H and B_{eq} as a function of the disorder strength W for fixed values of $J = 80$ meV, $L = 10.6$ nm and $R = 2.3$ nm.

are robust with respect to this loss of conductance, we now consider the effect of introducing an amount of scalar disorder in the samples. We do so by averaging over $N = 50$ Anderson disorder configurations in each of which we assign a random scalar on-site potential $W_i \in [-W/2 : W/2]$ to each atom in the quantum dot and tune the parameter controlling the disorder degree W from 0 to a maximum of ~ 400 meV, an upper limit for the energy scale associated with disorder that is consistent with the assumption of Coulomb long-range scattering.[42,49] The clean limit is recovered for $W = 0$.

We employ square leads and compare two disorder configurations with different symmetry: one where the disorder distribution preserves mirror symmetry with respect to the y axis and one where the distribution is completely random in the whole sample. A realization of each of these different disorder profiles is shown in fig. 5(a,b). Error bars associated with the standard deviation of the data are shown for completeness. From the resulting T_H curves shown in fig. 5(c,d) we see that symmetric disorder barely affects the Hall response of the problem, as it provokes changes in the normalized transmission imbalance of the order of $\Delta T_H/T_H \approx 10^{-2}$. On the other side, a randomly distributed disorder that does not respect $y \to -y$ symmetry affects the conductance more sizeably, yielding variations ΔT_H of the order of T_H. The difference could be explained by noting that in the symmetric case the defects simply act as a fluctuating potential that does not contribute to the asymmetry of the scattering, whereas in the random case an additional transverse conductance driven by the disorder asymmetry rather than by the skyrmion-induced AHE is generated. However, significant alterations of the Hall response only take place at relatively high values of the disorder potential of the order of ~ 400 meV, whereas for weaker and more reasonable disorder strengths the change in the conductance is smaller and comparable to the one obtained in the symmetric configuration. We can therefore safely rely on the results obtained so far for pristine graphene, as the unavoidable presence of a low concentration of defects and noise in the actual samples is not able to turn down the figure of merit of the problem.

V. CONCLUSIONS

Our results strongly indicate that graphene would be an excellent skyrmion detector at realistic exchange couplings of the order of $\sim$ 1-10 meV, exhibiting minimum Hall conductances G_H of the order of 10^{-5}-10^{-4} G_0, several orders of magnitude larger than the minimum experimentally detectable conductance of the order of 10^{-10} G_0.[50,51] The equivalent magnetic field $B_{\rm eq}$ can easily reach one Tesla for $J \approx 1$ meV , $R \approx 2$ nm and $L \approx 10$ nm. Besides, these values merely set a lower bound estimate for the conductances that are detectable in actual experimental devices where sample dimensions, skyrmion radius and even skyrmion number can be consistently larger than those considered in this work. Our results also show that at weak coupling Schrodinger electrons are less sensitive to the non-trivial magnetic ordering and respond with a conductance that is some orders of magnitude smaller than that displayed by Dirac electrons. Finally, we proved that scalar disorder does not affect the transverse conductance in a dramatic manner.

In conclusion, we suggest that graphene might be exploited as a non-invasive probe to readout the presence of an individual skyrmion in a material underneath. The underlying physical principle is the enhanced anomalous Hall effect due to the interaction of Dirac graphene fermions with non-coplanar spin textures. Our work establishes the principles of hybrid devices combining graphene Hall probes and insulating skyrmionic materials.[10–12]

ACKNOWLEDGMENTS

The authors acknowledge financial support by Marie-Curie-ITN 607904-SPINOGRAPH. JFR acknowledges financial supported by MEC-Spain (FIS2013-47328-C2-2-P and MAT2016-78625-C2) and Generalitat Valenciana (ACOMP/2010/070), Prometeo, by ERDF funds through the Portuguese Operational Program for Competitiveness and Internationalization COMPETE 2020, and National Funds through FCT- The Portuguese Foundation for Science and Technology, under the project PTDC/FIS-NAN/4662/2014 (016656). This work has been financially supported in part by FEDER funds. JLL and FF thank the hospitality of the Departamento de

Fisica Aplicada at the Universidad de Alicante. We are grateful to F. Guinea and P. San-Jose for useful discussions.

APPENDIX

A. Effects of the mismatch between graphene and the substrate

In this appendix we explore the effects of realistic perturbations in the quantum Hall conductance. In particular, we study (i) the moiré potential induced by the substrate, (ii) the renormalization effects on the exchange coupling between the graphene electrons and the substrate, associated to the mismatch between the two lattices, and (iii) the existence of a non-local component of the exchange interaction.

1. *Effect of onsite modulation*

The first effect captures the fact that a substrate with a lattice parameter that differs from that of graphene will result in the generation of a modulation of the local potential felt by the graphene electrons on a characteristic scale that depends on the lattice parameter of the underlying material. This could have important consequences on the magnitude of the anomalous response, since the existence of a moiré pattern could fold the Brillouin zone and generate intervalley scattering. We account for the effect of the potential modulation by means of the following contribution to the graphene Hamiltonian

$$H_m = \sum_i \mu_i c_i^\dagger c_i \quad \text{with} \quad \mu_i = \mu(\sum_j e^{-|\mathbf{r}_i - \mathbf{R}_j|/\Lambda} - \eta) \tag{18}$$

where we choose η such that $\langle \mu_i \rangle = 0$, that implies that the charge neutrality point is at $\varepsilon = 0$. For a fixed μ, the local potential μ_i varies within the interval $\mu_i \in [-\mu_{max}, \mu_{max}]$, depending on the value of Λ. Note that the limit $\Lambda \to \infty$ corresponds to the pristine case $\mu_i = 0$ for every site i. The vectors $\mathbf{R}_j$ indicate the positions of the atoms of the magnetic substrate, that we model as a triangular array[52] with a lattice parameter a_{tr} that is not commensurate with that of graphene, whereas the vectors $\mathbf{r}_i$ refer to the positions of the atoms in graphene. We take $\lambda = 0.5 a_0$ and we calculate the normalized transmission asymmetry as a function of $\mu_{max} = \max(\mu_i)$, and of the lattice parameter of the substrate a_{tr}. The results are shown in fig. 6(b) and (c), whereas in panel (a) we show a particular realization of the moiré pattern. We observe that even in the presence of sizable onsite modulations of 0.1 eV, the anomalous Hall signal remains at a similar magnitude as in the pristine case. Such behavior suggest that the anomalous Hall signal will be observable even in the presence of realistic substrate induced potentials.

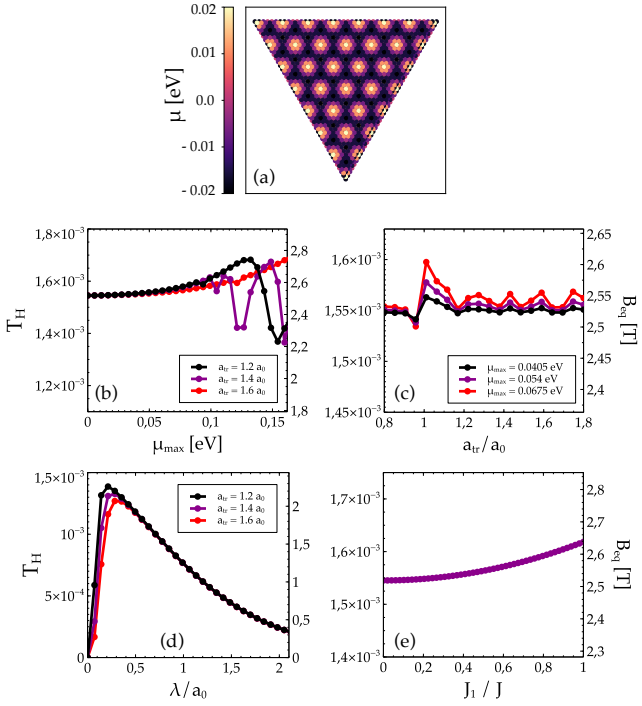

Figure 6. Panel (a) displays a specific configuration of the the site-dependent potential associated to the moiré pattern for $a_{tr} = 1.4\, a_0 = 3.44\, \AA$, $\Lambda = 0.3\, a_0 = 0.74$ nm and $\mu_{max} = 0.04$ eV. In panels (b) and (c) we study the effect of adding the term in eq. (18) to the Hamiltonian studied on the main text. Specifically, panel (b) shows T_H as a function of μ_{max} for different lattice parameters of the substrate, and panel (c) shows T_H as a function of a_{tr} for different values of μ_{max}. Both calculations are performed for $\Lambda = 0.5\, a_0$. In panel (d) we have substituted eq. (19) to the exchange Hamiltonian employed in the main text, equation (12), and calculated T_H as a function of λ for a fixed value of J and different values of a_{tr} . In (e) we show the behavior of the transmission asymmetry T_H as a function of the non-local exchange amplitude J_1/J when the Hamiltonian term in eq. (21) is added to eq. (12). All calculations were performed for an island with side of 10.6 nm, skyrmion radius of $R = 2.6$ nm, an exchange coupling constant of $J = 80$ meV and a distance between the graphene plane and the substrate $d = 2a_0$.

2. *Effect of exchange averaged over neighbors*

The second effect relates to the mismatch between the two lattices and accounts for the renormalization of the exchange coupling constant due to the fact that the exchange exerted by each localized magnetic moment of the substrate is not contact-like but rather decays exponentially over a distance of the order of the lattice parameter. Therefore, graphene electrons feel an exchange that is given by a superposition of the slightly misaligned magnetic moments of its nearest neighboring atoms in the substrate. In order to account for such an effect, we

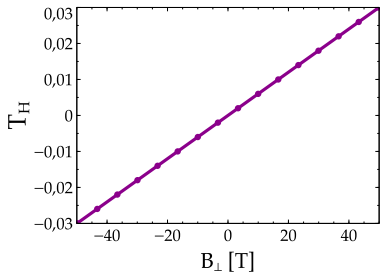

Figure 7. Normalized transmission imbalance $T_H = \delta T/T$ as a function of an applied perpendicular magnetic field $B_\perp$.

rewrite the exchange term of the Hamiltonian as

$$H_J = J \sum_i \mathbf{S}_i \cdot \langle \mathbf{n}_i \rangle(\lambda) \tag{19}$$

with $\langle \mathbf{n}_i \rangle(\lambda)$

$$\langle \mathbf{n}_i \rangle(\lambda) = \mathcal{C} \sum_j \mathbf{m}_j e^{-|\mathbf{r}_i - \mathbf{R}_j|/\lambda} \tag{20}$$

where j runs over the indexes of the substrate, $\mathbf{R}_j$ are the positions of the atoms of the substrate, $\mathbf{m}_j$ is a unit vector pointing in direction of the local magnetization on the sites of the substrate, and $\mathcal{C}$ is a normalization constant chosen so that $\max |\langle \mathbf{n}_i \rangle| = 1$. In the limit where graphene and the substrate are commensurate (if the substrate had also a honeycomb lattice), and $\lambda \to 0$, the previous formula would yield $\langle \mathbf{n}_i \rangle(\lambda) = \mathbf{m}_i$ and we would recover the contact-like and commensurate limit explored in the main text. Nevertheless, for non-commensurate lattices, the limit $\lambda \to 0$ would give exchange only in selected atoms, so that this regime is to be considered nonphysical in the present model. In any other situation, the previous parametrization yields a local exchange in graphene that it is a local average of the magnetization of the substrate, defined by the length scale λ. In the limit $\lambda \to \infty$, all the sites in graphene would feel the same exchange coupling, yielding a vanishing Hall response.

The result is shown in fig. 6(d) as a function of the range of decay λ, for three different values of a_{tr}. As is clear from this plot, T_H is of the order of the one that would be obtained for a contact-like interaction for small values of λ, and decays smoothly as λ increases. This behavior proves that a weighted average with the closest neighbors does not affect heavily the anomalous Hall signal, so that the local exchange interaction used through the main text is a fairly acceptable approximation.

3. *Effect of exchange mediated hopping*

The third effect studied accounts for the fact that non-local exchange interactions can also be present. In order to relax the assumption of purely local exchange, we introduce a term in the Hamiltonian that mimics the effect of an induced non-local exchange interaction. From a microscopic point of view, such term arises from electrons hopping from a carbon atom to a site in the skyrmion material, flipping their spin and hopping back to a different carbon atom in graphene. Such phenomena is accounted for by a spin dependent hopping term that we take to be the average between the induced onsite magnetization of the two sites involved. The non-local exchange Hamiltonian thus reads

$$H_{J_1} = J_1 \sum_{<i,j>} \mathbf{S}_{ij} \cdot \mathbf{n}_{ij} \tag{21}$$

where $\mathbf{S}_{ij} = \sum_{\sigma\sigma'} c^\dagger_{i\sigma} \mathbf{s}_{\sigma\sigma'} c_{j\sigma'}$ and $\mathbf{n}_{ij} = (\mathbf{n}_i + \mathbf{n}_j)/2$. In fig. 6(e) we show the behavior of the anomalous response with J_1/J, whence it appears evident that the signal is left almost unchanged by values of J_1 up to J. These three results are a strong indication that taking into account the presence of the lattice underneath the graphene sample does not affect in a sizable manner the strength of the anomalous signal, thus demonstrating the robustness of the results provided in the main text.

B. Determination of B_{eq}

In order to determine the equivalent magnetic field B_{eq}, we have performed a calculation of the transmission imbalance T_H of a three-terminal triangular device where a perpendicular magnetic field $B_\perp$ is applied to the transmission region. To include such field, we retain only the hopping term of eq. 12 where we perform the standard Peierls substitution $t \to t \exp\left(-i\frac{e}{\hbar}\int_{\mathbf{r}_i}^{\mathbf{r}_j} \mathbf{A} \cdot d\mathbf{r}\right)$ such that

$$H = -t \sum_{<i,j>,\sigma} c^\dagger_{i\sigma} c_{j\sigma} e^{-i\frac{e}{\hbar}\int_{\mathbf{r}_i}^{\mathbf{r}_j} \mathbf{A}\cdot d\mathbf{r}} \tag{22}$$

By calculating the transmission imbalance between left and right lead, one gets a linear relation $T_H \approx 20\, B_\perp$ as shown in fig. 7. The linear relation between $B_\perp$ and T_H, in the absence of a skyrmion, permit to assign an equivalent field $B_{\rm eq}$ to characterize the transmission imbalance calculated in the presence of a skyrmion at $B_\perp = 0$.

[1] U. K. Roszler, A. N. Bogdanov, and C. Pfleiderer, Nature **442** (2006).
[2] R. Duine, Nat Nano **8**, 800 (2013).
[3] A. Rosch, Nat Nano **12**, 103 (2017).
[4] B. Dupé, G. Bihlmayer, M. Böttcher, S. Blügel, and S. Heinze, Nature Communications **7**, 11779 EP (2016).
[5] Nat Nano **8**, 883 (2013).

[6] S. Mühlbauer, B. Binz, F. Jonietz, C. Pfleiderer, A. Rosch, A. Neubauer, R. Georgii, and P. Böni, Science **323**, 915 (2009).

[7] W. Münzer, A. Neubauer, T. Adams, S. Mühlbauer, C. Franz, F. Jonietz, R. Georgii, P. Böni, B. Pedersen, M. Schmidt, A. Rosch, and C. Pfleiderer, Phys. Rev. B **81**, 041203 (2010).

[8] X. Yu, N. Kanazawa, W. Zhang, T. Nagai, T. Hara, K. Kimoto, Y. Matsui, Y. Onose, and Y. Tokura, Nature communications **3**, 988 (2012).

[9] Y. Tokunaga, X. Yu, J. White, H. M. Rønnow, D. Morikawa, Y. Taguchi, and Y. Tokura, Nature communications **6** (2015).

[10] S. Seki, X. Yu, S. Ishiwata, and Y. Tokura, Science **336**, 198 (2012).

[11] M. C. Langner, S. Roy, S. K. Mishra, J. C. T. Lee, X. W. Shi, M. A. Hossain, Y.-D. Chuang, S. Seki, Y. Tokura, S. D. Kevan, and R. W. Schoenlein, Phys. Rev. Lett. **112**, 167202 (2014).

[12] S. Zhang, A. Bauer, H. Berger, C. Pfleiderer, G. van der Laan, and T. Hesjedal, Applied Physics Letters **109**, 192406 (2016).

[13] S. Heinze, K. von Bergmann, M. Menzel, J. Brede, A. Kubetzka, R. Wiesendanger, G. Bihlmayer, and S. Blugel, Nat Phys **7**, 713 (2011).

[14] N. Romming, A. Kubetzka, C. Hanneken, K. von Bergmann, and R. Wiesendanger, Phys. Rev. Lett. **114**, 177203 (2015).

[15] X. Z. Yu, Y. Onose, N. Kanazawa, J. H. Park, J. H. Han, Y. Matsui, N. Nagaosa, and Y. Tokura, Nature **465**, 901 (2010).

[16] C. Pfleiderer, Nat Phys **7**, 673 (2011).

[17] Y. Dovzhenko, F. Casola, S. Schlotter, T. X. Zhou, F. Büttner, R. L. Walsworth, G. S. Beach, and A. Yacoby, arXiv preprint arXiv:1611.00673 (2016).

[18] S. S. Parkin, M. Hayashi, and L. Thomas, Science **320**, 190 (2008).

[19] F. Jonietz, S. Mühlbauer, C. Pfleiderer, A. Neubauer, W. Münzer, A. Bauer, T. Adams, R. Georgii, P. Böni, R. A. Duine, K. Everschor, M. Garst, and A. Rosch, Science **330**, 1648 (2010).

[20] N. Nagaosa and Y. Tokura, Nat Nano **8**, 899 (2013).

[21] K. Hamamoto, M. Ezawa, and N. Nagaosa, Physical Review B **92**, 115417 (2015).

[22] G. Yin, Y. Liu, Y. Barlas, J. Zang, and R. K. Lake, Physical Review B **92**, 024411 (2015).

[23] J. L. Lado and J. Fernández-Rossier, Phys. Rev. B **92**, 115433 (2015).

[24] N. Nagaosa, J. Sinova, S. Onoda, A. H. MacDonald, and N. P. Ong, Reviews of Modern Physics **82**, 1539 (2010).

[25] J. Brede, N. Atodiresei, V. Caciuc, M. Bazarnik, A. Al-Zubi, S. Blügel, and R. Wiesendanger, Nature nanotechnology **9**, 1018 (2014).

[26] L. Banszerus, M. Schmitz, S. Engels, M. Goldsche, K. Watanabe, T. Taniguchi, B. Beschoten, and C. Stampfer, Nano letters **16**, 1387 (2016).

[27] N. M. Freitag, L. A. Chizhova, P. Nemes-Incze, C. R. Woods, R. V. Gorbachev, Y. Cao, A. K. Geim, K. S. Novoselov, J. Burgdorfer, F. Libisch, *et al.*, Nano Letters **16**, 5798 (2016).

[28] M. B. Shalom, M. Zhu, V. Falko, A. Mishchenko, A. Kretinin, K. Novoselov, C. Woods, K. Watanabe, T. Taniguchi, A. Geim, *et al.*, Nature Physics **12**, 318 (2016).

[29] A. Candini, C. Alvino, W. Wernsdorfer, and M. Affronte, Phys. Rev. B **83**, 121401 (2011).

[30] A. Candini, S. Klyatskaya, M. Ruben, W. Wernsdorfer, and M. Affronte, *Nano Letters*, Nano Letters **11**, 2634 (2011).

[31] J. W. González, F. Delgado, and J. Fernández-Rossier, Phys. Rev. B **87**, 085433 (2013).

[32] S. Zhang and S. S.-L. Zhang, Phys. Rev. Lett. **102**, 086601 (2009).

[33] G. E. Volovik, Journal of Physics C: Solid State Physics **20**, L83 (1987).

[34] Z. Qiao, S. A. Yang, W. Feng, W.-K. Tse, J. Ding, Y. Yao, J. Wang, and Q. Niu, Phys. Rev. B **82**, 161414 (2010).

[35] Ž. V. Šljivančanin, Z. S. Popović, and F. R. Vukajlović, Physical Review B **56**, 4432 (1997).

[36] A. H. Castro Neto, F. Guinea, N. M. R. Peres, K. S. Novoselov, and A. K. Geim, Reviews of Modern Physics **81**, 109 (2009).

[37] R. Landauer, *IBM Journal of Research and Development*, IBM Journal of Research and Development **1**, 223 (1957).

[38] M. L. Sancho, J. L. Sancho, J. L. Sancho, and J. Rubio, Journal of Physics F: Metal Physics **15**, 851 (1985).

[39] P. Wei, S. Lee, F. Lemaitre, L. Pinel, D. Cutaia, W. Cha, F. Katmis, Y. Zhu, D. Heiman, J. Hone, *et al.*, Nature materials (2016).

[40] H. X. Yang, A. Hallal, D. Terrade, X. Waintal, S. Roche, and M. Chshiev, Phys. Rev. Lett. **110**, 046603 (2013).

[41] Z. Qiao, W. Ren, H. Chen, L. Bellaiche, Z. Zhang, A. H. MacDonald, and Q. Niu, Physical Review Letters **112**, 116404 (2014).

[42] Z. Wang, C. Tang, R. Sachs, Y. Barlas, and J. Shi, Phys. Rev. Lett. **114**, 016603 (2015).

[43] A. A. Thiele, Physical Review Letters **30**, 230 (1973).

[44] F. Jonietz, S. Mühlbauer, C. Pfleiderer, A. Neubauer, W. Münzer, A. Bauer, T. Adams, R. Georgii, P. Böni, R. A. Duine, K. Everschor, M. Garst, and A. Rosch, Science **330**, 1648 (2010), http://science.sciencemag.org/content/330/6011/1648.full.pdf.

[45] K. Everschor, M. Garst, B. Binz, F. Jonietz, S. Mühlbauer, C. Pfleiderer, and A. Rosch, Physical Review B **86**, 054432 (2012).

[46] J. Sampaio, V. Cros, S. Rohart, A. Thiaville, and A. Fert, Nature nanotechnology **8**, 839 (2013).

[47] T. Okubo, S. Chung, and H. Kawamura, Physical Review Letters **108**, 017206 (2012).

[48] R. Wiesendanger, Nature Reviews Materials **1**, 16044 EP (2016).

[49] K. Nomura and A. H. MacDonald, Physical Review Letters **98**, 076602 (2007).

[50] A. Tzalenchuk, S. Lara-Avila, A. Kalaboukhov, S. Paolillo, M. Syväjärvi, R. Yakimova, O. Kazakova, T. Janssen, V. Fal'Ko, and S. Kubatkin, Nature nanotechnology **5**, 186 (2010).

[51] B. Jeckelmann and B. Jeanneret, Reports on Progress in Physics **64**, 1603 (2001).

[52] L. Schmidt, J. Hagemeister, P.-J. Hsu, A. Kubetzka, K. von Bergmann, and R. Wiesendanger, New Journal of Physics **18**, 075007 (2016).